PNAS RESEARCH ARTICLE | EARTH, ATMOSPHERIC, AND PLANETARY SCIENCES

Patagonian dust, Agulhas Current, and Antarctic ice-rafted debris contributions to the South Atlantic Ocean over the past 150,000 years

Anne E. Barkley[a,1,2], Gisela Winckler[a,b,1], Cristina Recasens[a], Michael R. Kaplan[a,1], Bess G. Koffman[c], Fernando Calabozo[d], Jennifer L. Middleton[a], Robert F. Anderson[a,b], Yue Cai[e], Louise Bolge[a], Jack Longman[f,g], and Steven L. Goldstein[a,b,1]

Affiliations are included on p. 11.

Edited by Eric Rignot, University of California Irvine, Irvine, CA; received January 30, 2024; accepted June 12, 2024

Disentangling inputs of aeolian dust, ice-rafted debris (IRD), and eroded continental detritus delivered by ocean currents to marine sediments provide important insights into Earth System processes and climate. This study uses Sr-Nd-Pb isotope ratios of the continent-derived (lithogenic) fraction in deep-sea core TN057-6 from the subantarctic Southern Ocean southwest of Africa over the past 150,000 y to identify source regions and quantify their relative contributions and fluxes utilizing a mixing model set in a Bayesian framework. The data are compared with proxies from parallel core Ocean Drilling Program Site 1090 and newly presented data from potential South America aeolian dust source areas (PSAs), allowing for an integrated investigation into atmospheric, oceanic, and cryospheric dynamics. PSA inputs varied on glacial/interglacial timescales, with southern South American sources dominating up to 88% of the lithogenic fraction (mainly Patagonia, which provided up to 68%) during cold periods, while southern African sources were more important during interglacials. During the warmer Marine Isotope Stage (MIS) 3 of the last glacial period, lithogenic fluxes were twice that of colder MIS2 and MIS4 at times, and showed unique isotope ratios best explained by Antarctic-derived IRD, likely from the Weddell Sea. The IRD intrusions contributed up to 41% at times and followed Antarctic millennial warming events that raised temperatures, causing instability of icesheet margins. High IRD was synchronous with increased bioavailable iron, nutrient utilization, high biological productivity, and decreased atmospheric CO_2. Overall, TN057-6 sediments record systematic Southern Hemisphere climate shifts and cryospheric changes that impacted biogeochemical cycling on both glacial/interglacial and subglacial timescales.

ice-rafted debris | dust | Southern Ocean | provenance | climate

Significance

The continent-derived (lithogenic) portion of seafloor sediments contains information useful for understanding past climate. This study uses geochemical-isotopic fingerprinting to determine the source of lithogenic material in a core from the subantarctic Atlantic since 150,000 BP. Results show the predominant source was Patagonian dust during ice ages, while Southern Africa was more important during warm ages, reflecting ice-age gustiness. Moreover, during the warm interval of the last ice age from 55,000 to 35,000 BP, increased fluxes of ice-rafted debris (IRD) to the site followed Antarctic warm events, which raised temperatures and caused instability in Antarctic ice sheets. Increased biological productivity instigated by bioavailable iron from IRD may explain synchronous increases in productivity and could have contributed to decreased atmospheric CO_2.

Across the planet, marine and ice core records show aeolian dust fluxes varied synchronously throughout the late Quaternary (1–3). Such changes in atmospheric dust loadings can alter the radiative balance of the atmosphere and influence carbon uptake through ocean fertilization (4, 5). In addition to aeolian dust, marine sediments archive eroded continental detritus transported via ocean currents and ice-rafted debris (IRD) from the melting of sediment-laden icebergs. The composition of the total continent-derived (lithogenic) component of marine sediments thus reflects a variety of Earth System processes (6, 7), with atmospheric circulation delivering the dust component, ocean currents delivering eroded continental detritus, and icebergs delivering IRD. Therefore, changes in eroded detrital and IRD fluxes do not necessarily mirror changes in dust fluxes because they are not governed by the same processes. The source regions of these assorted lithogenic inputs can be identified by geochemical provenance fingerprinting utilizing the products of long-lived radioactive decay (e.g., refs. 8–11), thereby shedding light on how fluctuating climatic conditions affect different but integrated Earth System processes.

Despite its climatic importance, Southern Hemisphere (SH) provenance studies have been limited, particularly in the South Atlantic, where they have mainly focused on climatic changes between the Last Glacial Maximum (LGM) and the present day (12–14). In this work, we present a 150 ka high-resolution isotopic fingerprint record of lithogenic inputs to core site TN057-6 (42°54′S, 8°54′E, 3,751 m) in the subantarctic Southern Ocean southwest of Africa. This core and the parallel Ocean Drilling Program (ODP) Site 1090 are well dated (15, 16) and ideally situated for distinguishing between possible inputs to obtain an integrated picture of SH climate. Both are located downwind of southern South American (SSA) dust sources (17), and far from the African coast, on the elevated topography of the Agulhas Ridge far above the deep

[1]To whom correspondence may be addressed. Email: barkley.anne@epa.gov, winckler@ldeo.columbia.edu, mkaplan@ldeo.columbia.edu, or steveg@ldeo.columbia.edu.

[2]Present address: The Center for Public Health and Environmental Assessment, Office of Research and Development, U.S. Environmental Protection Agency, Washington, D.C. 20004.

This article contains supporting information online at https://www.pnas.org/lookup/suppl/doi:10.1073/pnas.2402120121/-/DCSupplemental.

Published July 23, 2024.

Cape Basin abyssal plain, which isolates the site from direct continental riverine inputs from southwest Africa and horizontal abyssal flow of sediment by bottom currents. Previous studies of ODP 1090 found a tight coupling between nutrient utilization and dust-delivered iron (Fe) that increased the efficiency of the biological pump during glacial periods and may have been responsible for an up to 40 ppm reduction in global atmospheric carbon dioxide (CO_2) concentrations (18–20). These studies extrapolated the results from this site to the whole Southern Ocean, highlighting the importance of TN057-6/ODP 1090 as a core/drill site for understanding SH climate.

Records from SH marine sediments and Antarctic ice cores show synchronous increases in dust fluxes during glacial periods (2, 3, 16). Previous provenance work in Antarctic ice cores concluded that Patagonia was a major source of dust during glacial periods (21–23), and this dust would also pass over the southeast Atlantic Ocean. These glacial increases may reflect changes in the conditions that led to variations in glacier activity or in atmospheric circulation strength over SSA. A possible explanation for Patagonian dominance during glacial periods is glaciogenic dust generation in the Andes, which can include glacial meltwater deposition of fine-grained material onto outwash plains that is easily mobilized (24). High dust flux intervals within Antarctic dust flux records have been linked to periods when this process was known to occur (25). Additionally, increased glacial dust supply may have been driven by enhancement in the strength of atmospheric circulation in the SH through stronger Southern Westerly Winds together with reduced dust removal via wet deposition by precipitation (26, 27). By identifying the provenance of lithogenic material delivered to the southeast Atlantic, we examine these hypotheses and extend our record beyond the LGM to 150 ka.

Changes in IRD fluxes at proximal or distal core sites provide information about past ice sheet dynamics. IRD records have been used extensively to reconstruct Northern Hemisphere ice sheet variability, which has led to profound insights into millennial-scale climate states such as Heinrich Events reflecting major iceberg production (9). However, less is known about the SH (28), especially prior to the LGM, hindering our understanding of Antarctic ice sheet dynamics and climate. IRD serves as a proxy for iceberg activity over a core site, with increased IRD indicating more icebergs. For example, increased IRD in the Scotia Sea has been linked to greater ice sheet instability during the last deglaciation (6). Periods of icesheet instability are of great interest as the growth and shrinking of ice sheets have large impacts on global sea level, which is particularly relevant in the South Atlantic region today given the sensitivity of the West Antarctic Ice Sheet (WAIS) to warming.

Moreover, aeolian dust or IRD fluxes provide nutrients that can stimulate primary productivity in the Fe-limited Southern Ocean (29). However, different lithogenic sources show different Fe solubilities and provide differing amounts of bioavailable Fe (30, 31). While geochemical fingerprinting can be used to understand climate processes by resolving provenance and source type, such information can also aid in predicting "downstream effects" on climate by quantifying associated nutrients and solubilities. For example, dust or IRD from certain types of crystalline rock sources in Patagonia that are affected by glacial activity contains high amounts of soluble (or bioavailable) Fe. This is because glacially ground crystalline basement is generally less chemically weathered than chemically altered sediment from arid regions, and thus contains Fe in its reduced (+2) form (32). IRD has been shown to be an excellent source of bioavailable Fe that can cause increases in primary production (33, 34). While there are many biological and physical controls on the carbon cycle (35), increases in IRD and glacially ground aeolian dust can promote increased primary production, resulting in decreased atmospheric CO_2.

The ability to distinguish between dust, eroded continental material, and IRD refines our capacity to interpret the oceanographic and climatic conditions recorded in sediments. This study compares the Sr-Nd-Pb isotopic compositions of the fine particulate (<5 μm-sized) lithogenic material in TN057-6 to potential SH sediment sources and evaluates the provenance of the core samples using a mixing model set in a Bayesian framework to quantify the relative proportions of sediment and lithogenic flux contributions from each source. Our results reveal insights into glacial/interglacial and suborbital changes in SH atmospheric and oceanic dynamics and ice sheet stability, which we connect to biogeochemical cycles and changes in atmospheric CO_2, coalescing in a cohesive perspective on the global impacts of SH climate change.

Results and Discussion

We present a high temporal resolution (averaging 2 to 3 ky overall) dataset of Sr, Nd, and Pb isotope ratios of the <5 μm fraction of the lithogenic component from core TN057-6 over the past 150 ka (Figs. 1–3 and Dataset S1). The isotopic compositions vary on glacial/interglacial timescales in general (Figs. 2 and 3) and on suborbital timescales during Marine Isotope Stage (MIS) 3, when peak lithogenic fluxes were twice that of the LGM (Figs. 4 and 5). During MIS3, sampling resolution is increased to ~1 ky to identify the climatic patterns driving the high fluxes, and MIS3 is considered separately in the following discussion.

The potential source areas (PSAs) included in this study are two regions in southern South America (SSA), Southern Africa, and Antarctica. Similar to the core samples, only the <5 μm fraction was used in order to account for the influence of grain size on Sr isotope ratios (42), which tend to be higher in samples with small particle size because clays and micas often have high Rb/Sr ratios, and taking into account that wind-blown dust is composed of the fine fraction of the sources. In SSA, Patagonia has been shown to be a substantial aeolian dust source to Antarctica (21) and the Atlantic sector of the Southern Ocean (12, 13). Here, we define the Patagonian endmember (n = 129) as all areas in SSA south of 32°S (13, 21, 23). This endmember includes 55 new Patagonian PSA samples (*SI Appendix*, Fig. S1 and Dataset S2) used to better define the variability of glacial-related sediments (25). The region to the north of Patagonia between 32°S and 22°S has been shown to impact Antarctic ice core records (23) and may be the dominant dust source in the Pacific sector of the Southern Ocean (43, 44). Our study labels this as the Northern SSA endmember (n = 16), and it includes the northern and southern Puna and northern and middle Central Western Argentina PSAs defined in previous studies (23, 42, 43, 45, 46). The Southern Africa endmember (n = 8) is composed of material that originates from the Archean and Proterozoic terrains in southeastern Africa (e.g., ref. 46), which is then carried by rivers to the surface-flowing Agulhas Current and subsequently to the southeast Atlantic (10, 12). The isotopic compositions of this endmember are defined by eight newly measured samples on the <5 μm fraction from four cores located beneath the Agulhas Current (Dataset S1), which are similar to the Southern Africa endmember defined in Franzese et al. (10) for Nd and Sr isotopes. The samples used to define the Antarctic endmember (n = 10) originate from the bedrock surrounding the Ross Sea (6, 37), although, as discussed below, we interpret results to represent IRD sourced from the southern Weddell Sea. Australia and New Zealand were excluded as PSAs because they do not have substantially similar isotopic compositions to our marine core samples except during the Holocene (43, 44, 47, 48). Material from the Orange and Olifant Rivers in southwestern Africa was also excluded from our analysis as previous work ruled out these sources based on isotopic evidence

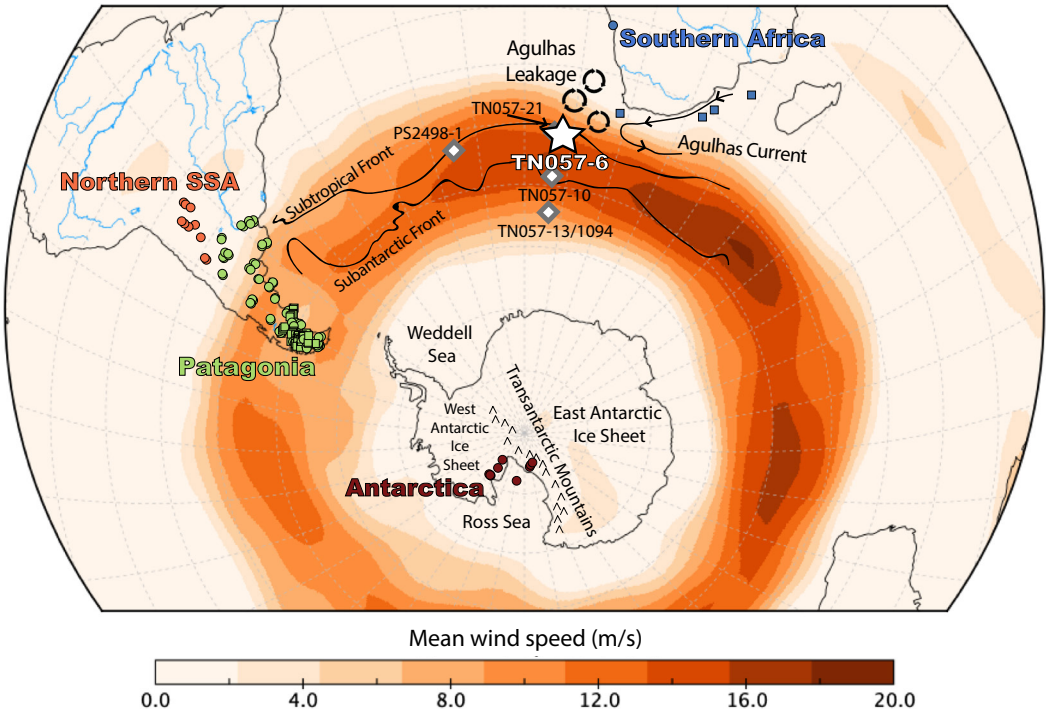

Fig. 1. Schematic of SH in relation to core TN057-6/ODP 1090 (star). The gray diamonds show the locations of PS2498-1, TN057-21, TN057-10, and TN057-13/IODP 1094. Background shading depicts mean 850 hPa wind speed (m s^{-1}) from 1948 to 2022 from NCAR/NCEP Reanalysis. PSAs of lithogenic material delivered to TN057-6 are shown with colored markers where circles represent previously published samples and squares represent new source data presented in this work. Circles with arrows near southern Africa represent Agulhas Leakage from the Agulhas Current. This figure was made in part using NASA's Panoply software version 5.2.3 (https://www.giss.nasa.gov/tools/panoply/).

showing no major contribution at core sites much closer to the African coast (10, 12) than TN057-6, which is located >1,200 km from Cape Town, South Africa. Additional details about methods are found in the *Methods and Materials* and *SI Appendix* sections. The average PSA isotopic composition and concentration data are in *SI Appendix*, Tables S1 and S2, respectively.

To quantify our provenance results, we employ an isotopic mixing model set in a Bayesian framework to quantify the relative proportion of sediment that originates from each source (44, 49). Model simulations were run using informative priors, meaning all relevant information was used, including isotopic composition and additional paleoclimate proxy records, to obtain more accurate posterior distributions. In practice, this means PSA endmembers were only considered for runs when isotopic and additional proxies suggested that the source contributed. Therefore, Patagonia, Northern SSA, and Southern Africa endmembers are included as PSAs throughout all time periods. During only MIS3, we additionally include Antarctica based on isotopic similarities between MIS3 samples and the Antarctic endmember, as well as on other supporting evidence including, but not limited to, grain size and n-alkane fluxes. The MIS3 section below contains the full rationale.

The isotopic mixing model was run for individual samples (Fig. 3 *D* and *E*) and for time periods (e.g., interglacials, glacials, MIS3, and MIS2), which was done by averaging the isotopic ratios during each time period. The fractions contributed by each PSA are reported as midpoints of the highest density 95% credible interval for individual samples (Fig. 3*D*), where the error bars in Fig. 3*D* represent the lower and upper values of the credible interval. We calculated the lithogenic flux from each source by multiplying each PSA fraction by the total lithogenic flux represented by the bulk sample (Fig. 4*A*) based on the ^{230}Th-normalized ^{232}Th abundance (i.e., assuming the ^{232}Th represents the lithogenic fraction, which is available for ~5 to 100 ka), adjusted for the typical ^{232}Th concentrations in the individual regions. The results of these flux-by-source calculations are presented in Fig. 3*F*, in which the error bars in Fig. 3*F* represent the lower and upper values of the credible interval.

Lithogenic Sources to the Southeast Atlantic. Sr-Nd-Pb isotope ratios of all the TN057-6 samples fall between the Patagonia, Northern SSA, Southern Africa, and Antarctica endmembers (Fig. 2). The samples from interglacial MIS1 and 5, and glacial MIS2, 4, and 6, fall on an array that broadly trends between Patagonia (with the highest Nd and lowest Sr and Pb isotope ratios) and Southern Africa (with the lowest Nd and highest Sr and Pb isotope ratios). As detailed in the *Methods and Materials* section, Nd isotope ratios are presented as ε_{Nd}, the deviation of the measured ^{143}Nd/^{144}Nd ratio in a sample from an estimate of the average value of the solar system, in parts per 10,000. The interglacial samples show values closer to the Southern Africa endmember and the glacial samples are closer to Patagonia. The samples from MIS3 are offset from the broad glacial/interglacial trend. In light of the MIS3 differences, in this study "glacial" refers to MIS2, 4, 6, excluding MIS3.

The lower Nd isotope ratios (average ± 1σ) of interglacial samples (ε_{Nd} = −9.4 ± 0.5) compared with glacial samples (ε_{Nd} = −7.2 ± 0.7) indicate older continental sources for the interglacial lithogenic material (50), consistent with the crustal ages of Southern Africa vs. South America, respectively (Fig. 2). The interglacial samples also show higher average Sr and Pb isotope ratios compared to glacial periods (^{87}Sr/^{87}Sr = 0.721 ± 0.002 vs. 0.715 ± 0.002; ^{206}Pb/^{204}Pb = 18.96 ± 0.04 vs. 18.86 ± 0.04; respectively). In detail, the glacial/interglacial isotopic trend falls off the binary Patagonia-Southern Africa mixing lines, which shows that the samples include inputs from at least one more source.

Interglacial samples fall above the Patagonia-Southern Africa mixing curve in Sr-Nd and Pb-Nd space (Fig. 2 *A* and *B*) and below the mixing curves in Pb-Nd and Pb-Pb space (Fig. 2 *C* and *D*). Samples from glacial periods fall on the same broad isotopic array as samples from interglacial periods but are shifted closer to the Patagonian

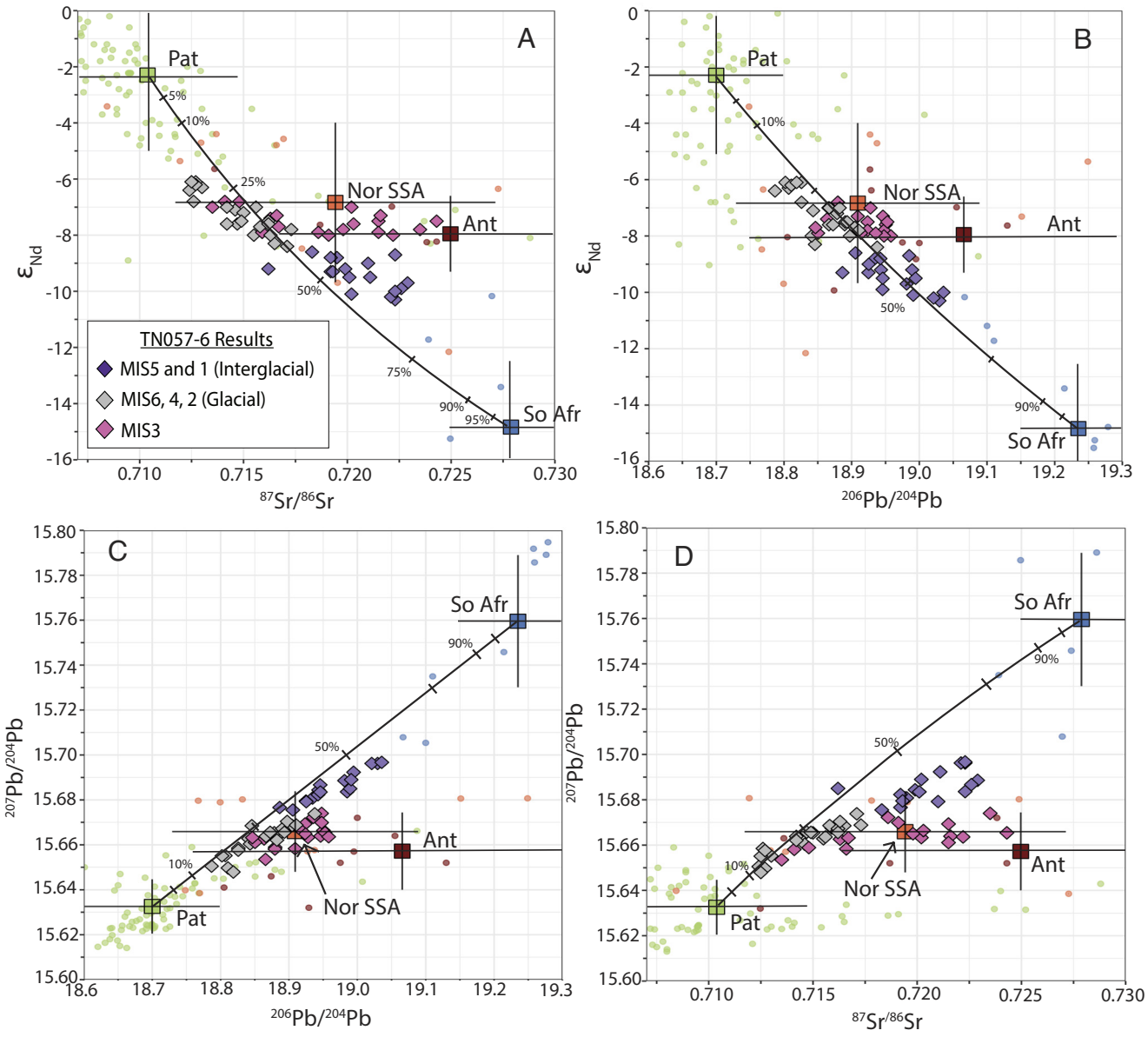

Fig. 2. Sr-Nd-Pb isotope results from TN057-6 and PSAs (*A*–*D*). Results from the <5 μm grain size fraction from core site TN057-6 showing combinations of Sr-Nd-Pb isotope ratios from this study (filled diamonds) with color indicating MIS. Previously published PSA samples and new samples presented in this work from PSAs are shown in the small circles while square markers with error bars represent the mean and 1σ of the data from each PSA. Note that some circles fall outside the domain of each plot. The black lines show the binary mixing curve between Patagonia and Southern Africa endmembers with hash marks at 5, 10, 25, 50, 75, 90, and 95%. Endmember abbreviations: Pat is Patagonia (>32°S); Nor SSA is Northern Southern South America (22°S to 32°S); Ant is Antarctica; So Afr is Southern Africa.

endmember. Both glacial and interglacial samples are "pulled off" the mixing curve toward the Northern SSA endmember, and we suggest the main array is dominated by those three components.

Mixing model results indicate for interglacial periods nearly equal contributions from Southern Africa (34 to 35%) and Patagonia (34 to 36%) (Fig. 3 *D* and *E*). In contrast, Patagonia delivered a much higher lithogenic fraction during glacial periods (57 to 59% during all glacials and 66 to 68% during MIS2). The Northern SSA source provided about a fifth of the total throughout (18 to 20% during interglacials, 21 to 23% during glacial periods, and 18 to 21% during MIS2). This means that more than half of the lithogenic fraction to the southeast Atlantic during interglacials (up to 56%) originated from SSA (Patagonia and Northern SSA together), and that SSA predominates during glacials (up to 82% during all glacial periods, and up to 88% during MIS2). Meanwhile, Southern Africa contributed just 15 to 16% during glacial periods and its flux remains relatively constant throughout the last ~100 ka during both glacial and interglacial periods. Reflecting the decrease in the flux from Patagonia during interglacials, and the near constancy of the Northern SSA flux, the proportion of the Southern Africa-derived lithogenic fraction during interglacials rises to 34 to 35% (but peaked up to ~48% at ~116 ka).

Enhanced Agulhas Leakage Signal during Interglacial Periods (MIS5 and Holocene). Our interpretation is similar to that of Franzese et al. (10, 12, 51), who concluded that the SSA signal dominates during glacials and the Southern African signal is higher during interglacials. They concluded that the African-derived material originates from rivers that flow out of southeastern Africa and is delivered to the Cape Basin by the surface-flowing Agulhas Current, whereas they ruled out riverine runoff from southwestern African rivers (12). They also concluded that the variability of the Southern Africa signal reflects the flux of the Agulhas Leakage into the South Atlantic, and this increases during interglacials. As discussed above, we found the relative contribution from Southern African sources is 34 to 35% during interglacials but

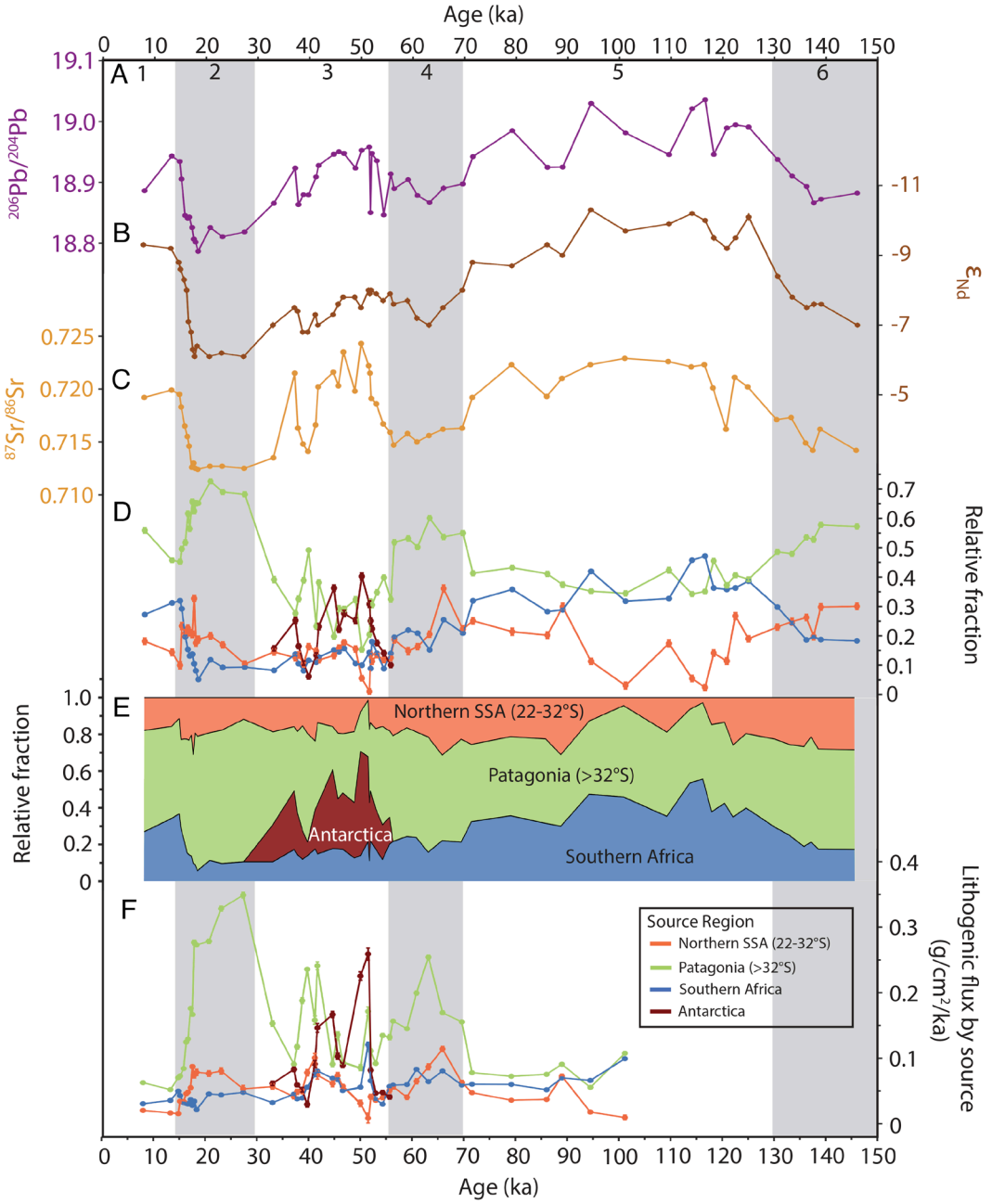

Fig. 3. Time series of the Sr, Nd, and Pb isotope ratios of the <5 μm grain size in samples from TN057-6, the relative PSA contributions, and PSA lithogenic fluxes. (*A*) $^{206}Pb/^{204}Pb$. (*B*) Neodymium (Nd) values expressed as ε_{Nd}. (*C*) $^{87}Sr/^{86}Sr$. 2σ errors are plotted in (*A*–*C*) but are generally smaller than the markers. (*D*) Relative contribution estimated by the MixSIAR mixing model. The error bars show the range of the highest density 95% credible interval, and the circle marker shows the midpoint of this interval. (*E*) Relative contributions estimated by the source apportionment MixSIAR model. (*F*) TN057-6 lithogenic flux from each PSA, derived from the ^{230}Th-normalized ^{232}Th flux multiplied by the relative contribution estimated by the source apportionment MixSIAR shown in (*D*) and adjusted for Th concentrations of each source area [Northern SSA (22°S to 32°S) = 13 ppm (36); Patagonia (>32°S) = 9 ppm from ref. 36; Southern Africa assumed global mean of 11 ppm; and Antarctica = 17 ppm (37)].

peaked to up to 48% at ~116 ka during MIS5. Assuming a ^{232}Th concentration of 11 ppm, we found the average flux of material from the Southern Africa source was 0.06 g cm^{-2} ka^{-1} during interglacials. Southern Africa also shows the lowest variability among the endmembers and contributed between 0.03 and 0.10 g cm^{-2} ka^{-1} over the past ~100 ka (Fig. 3*F*).

Thus, our flux-by-source calculations show little variability in Southern African contribution across the past ~100 ka. Our results could mean that the strength of the Agulhas Current did not change on glacial/interglacial timescales and therefore would not have affected Agulhas Leakage and the contribution of material to our site. However, this explanation contradicts findings that the Agulhas Current increased in strength during past deglacial periods (52). Alternatively, changes in the strength of Agulhas Leakage could have been offset by the amount of sediment carried by the Agulhas Current. For example, if the Agulhas Leakage was weaker during glacial periods, the weakening could be offset by higher river runoff from the Zambezi and Limpopo Rivers, whose length spans from southwestern to southeastern Africa, that flow into the Agulhas Current due to higher precipitation and a wetter Southern African climate. This explanation is supported by studies showing Africa's winter rainfall zone expanded and led to more precipitation during glacial periods in southern Africa (53–56).

Increased aeolian dust input sourced from southwestern Africa could present an alternative explanation for increased Southern African contributions during interglacials, as recently concluded

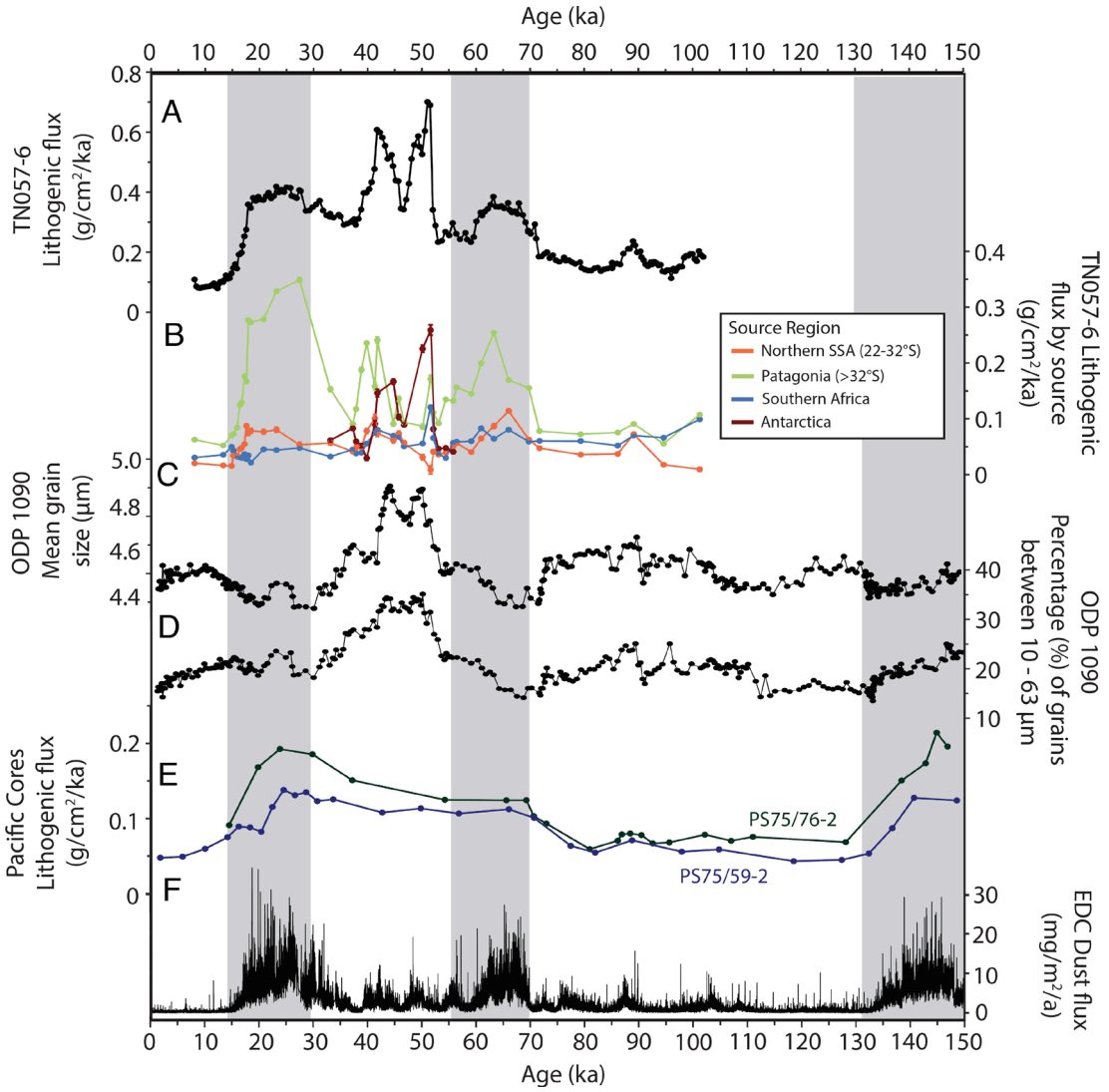

Fig. 4. Time series comparing TN057-6 fluxes to ODP 1090 grain sizes, Pacific Ocean lithogenic fluxes, and Antarctic dust flux. (*A*) Total lithogenic flux, calculated from the ^{230}Th-normalized ^{232}Th flux measured at TN057-6 (16). (*B*) Lithogenic flux of PSAs as shown in Fig. 3*F*. (*C*) Mean grain size (µm) measured from parallel core ODP 1090 (38). (*D*) Percentage of grain sizes between 10 and 63 µm from parallel core ODP 1090 (38). (*E*) Lithogenic flux, calculated from the ^{230}Th-normalized ^{232}Th flux measured at PS75/76-2 and PS75/59-2 in the Pacific Ocean (2). (*F*) EDC Antarctic dust flux (3).

by an isotopic provenance study of an East Antarctic ice core (57). While some southwestern African dust may have contributed material to TN057-6, we conclude that the Agulhas Leakage is a more likely explanation as the major Southern Africa source, due in part to the mismatch between interglacial samples and most SW African source material (*SI Appendix*, Fig. S3). While fine material from the Namibian Huab region overlaps with the isotopic compositions of eroded continental detritus associated with the Agulhas Current, most southwestern Africa dust sources have differing Pb ratios. In Pb isotope space, samples from interglacial periods fall closer to a binary mixing curve between Patagonia and southeastern Africa rather than between Patagonia and southwestern Africa (*SI Appendix*, Fig. S3).

Patagonian Dust as the Dominant Source of Lithogenic Material during Glacial Periods. As discussed in a previous section, Patagonia delivered up to 59% of the lithogenic material during glacial periods and up to 68% during MIS2. Peak contributions from Patagonia of 73% occurred at ~21 ka (Fig. 3 *D* and *E*). The Northern SSA source provided ~20% during glacial periods including MIS2, meaning SSA sources together provided up to 82% of the total to the southeast Atlantic during glacial periods and up to 88% during MIS2. Flux-by-source calculations show the average lithogenic flux from Patagonia during glacial periods was 0.20 g cm^{-2} ka^{-1}. The average lithogenic flux from Patagonia during MIS2 was 0.22 g cm^{-2} ka^{-1}, peaking at 0.35 g cm^{-2} ka^{-1} at 27 ka. Both Patagonia and Northern SSA sources together provided nearly 0.30 g cm^{-2} ka^{-1} during glacial periods and MIS2 (Fig. 3*F*).

Our isotopic data thus show that wind-carried dust from Patagonia has been by far the dominant source of lithogenic material delivered to the southeast Atlantic during glacials (Fig. 3 *D*–*F*), which is also the case for Antarctica based on ice core data (8, 23). As our results show consistent patterns across the past three glacial maxima (Fig. 2), we also conclude that there were consistent systematic changes during glacials that led to increases in these lithogenic fluxes. Patagonian dust domination of the isotopic signature of the southeast Atlantic is likely due to a combination of factors. These include TN057-6 being located directly downwind from Patagonia and under the South American dust plume, as estimated by paleoclimate models (17, 58). Additionally, glacial processes could have contributed to the increase in material from Patagonia as expanding glaciers and outwash plains provided fine-grained sediment that can be easily mobilized by winds (25). This assertion is consistent with data from ODP 1090 showing a decrease in

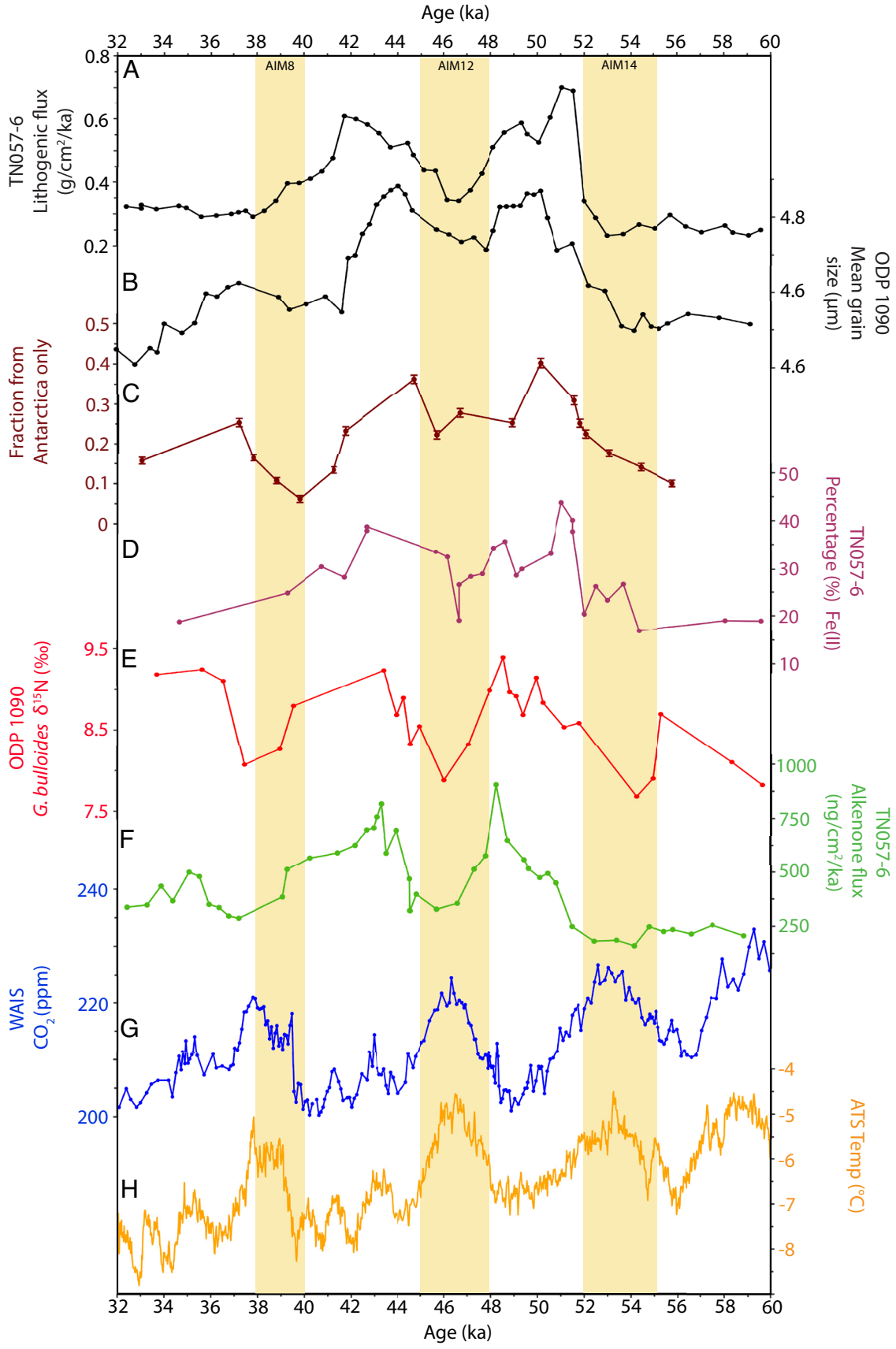

Fig. 5. Comparison of proxy time series for 60 to 32 ka, bounding the MIS3 "camel hump" interval. (*A*) TN057-6 total lithogenic flux as shown in Fig. 4*A* (16). (*B*) Mean grain size measured from parallel core ODP 1090 (38). (*C*) Mixing model results depicting the relative proportion of material from the Antarctica PSA where the error bars represent the range of the highest density 95% credible interval. (*D*) Relative fraction of Fe(2+) measured from TN057-6 (32). (*E*) *G. bulloides* FB-δ^{15}N measured from ODP 1090 (18). (*F*) ^{230}Th normalized alkenone flux from TN057-6 (18). (*G*) Atmospheric carbon dioxide (CO_2) measured in the WAIS Divide ice core (39). (*H*) Antarctic temperature record from Antarctic Temperature Stack (ATS) (40). Vertical yellow boxes represent the major AIM events during this interval (41).

mean grain size during glacial periods (Fig. 4*C*), potentially reflecting larger contributions from fine-grained glacial flour (38).

An interesting nuance to our isotopic record is that samples from MIS2 are situated closer to the Patagonian endmember than MIS6 or MIS4 samples (*SI Appendix*, Fig. S4). This points to Patagonia as a particularly important source of dust during the LGM though it is not clear why. One explanation could be that some areas (i.e., not all of Patagonia) exhibited slightly larger glaciations during MIS2 relative to MIS4, which could have generated more dust (e.g., ref. 59).

Our results further support a role for Patagonia as the dominant source of lithogenic material during glacial maxima that could have contributed to the lowering of atmospheric CO_2 (18). In line with conclusions from Shoenfelt et al. (32) and supported by grain-size data from van der Does et al. (38), our results strongly suggest that the higher Fe solubilities measured during glacial periods at TN057-6 were indeed driven by dust from Patagonian glacial activity.

Our results showing that Patagonia is the dominant dust source, along with contributions from Northern SSA during glacial periods, agree with modeling studies (17, 58) and geochemical data from Antarctic ice cores (21, 23, 25, 42, 60). In contrast, our results differ from provenance studies in the Pacific Ocean that indicate ~60% of the lithogenic flux originates from SSA north of Patagonia (similar to our Northern SSA endmember) (47). This difference may be due to the geographic location of TN057-6 being directly downwind of Patagonia.

Contributions to the Lithogenic Flux from Antarctic IRD during MIS3. The MIS3 data are unique in several ways. One striking feature of the TN057-6 lithogenic flux record, also reflected in the ^{232}Th flux, are two peaks ("camel humps") occurring at ~52 and ~42 ka (Fig. 4*A* and *SI Appendix*, Fig. S5). Both the magnitude and temporal pattern are observed across the South Atlantic at two additional core sites, one on the Mid-Atlantic Ridge (PS2498-1) and at TN057-21 (16) (the site survey core for IODP Site 1089), located near TN057-6 (Fig. 1), but deeper and on the abyssal plain. The lithogenic flux at each MIS3 camel hump at TN057-6 is approximately twofold greater than the average LGM flux. Additionally, MIS3 fluxes increased rapidly from ~0.25 to 0.69 g cm^{-2} ka^{-1} within ~2 ky between 53 and 51 ka as well as from ~0.35 to nearly 0.61 g cm^{-2} ka^{-1} between 46 and 42 ka, far faster than between glacial/interglacial cycles. These high fluxes are surprising, in part, because glacial periods generally experience the highest dust loadings while MIS3 globally shows only intermediate dust input based on dust in ice cores (3) (Fig. 4*F*). Both of these patterns suggest a rapid and repeated climate shift occurred during MIS3 that drove enhanced lithogenic fluxes, impacting a large portion of the South Atlantic extending from 53°S to 42°S in the Southern Ocean (61).

MIS3 samples also have unique isotopic compositions compared to other time intervals. Their isotopic compositions fall far off the Patagonia-Southern Africa binary mixing curve (Fig. 2). They also fall far off the trend of the other TN057-6 samples. While their ε_{Nd} values show a small range, between ~−7 and −8, they show a large range of $^{87}Sr/^{86}Sr$ ratios between ~0.713 and ~0.725, and include the highest $^{87}Sr/^{86}Sr$ ratios in the dataset. MIS3 samples show nearly uniform $^{207}Pb/^{204}Pb$ ratios (~15.66), with $^{206}Pb/^{204}Pb$ (~18.8 to 19.0) and $^{208}Pb/^{204}Pb$ (~38.8 to 39.0) offset to slightly higher values compared to the trends shown by the other TN057-6 samples (Fig. 2 *B*–*D* and *SI Appendix*, Fig. S2). The unique compositions in Sr-Nd-Pb isotope space require an additional unique source for the MIS3 lithogenic fraction.

Multiple lines of evidence point to Antarctic IRD as the missing sediment source. Our Antarctic endmember is defined by intermediate ε_{Nd}-values (~−8) compared to Patagonia and Southern Africa (~−2 and −15, respectively) with $^{87}Sr/^{86}Sr$ offset to high values compared to the Patagonia-Southern Africa mixing array, like the MIS3 samples. Moreover, the combination of Pb isotope ratios also fits the Antarctic source (Fig. 2 and *SI Appendix*, Fig. S2) (37). Thus, the Sr-Nd-Pb isotope ratios of the Antarctic source satisfy the isotopic mass balance needed to explain MIS3 samples. When included in our mixing model, results show that the Antarctic source contributed 19 to 21% (and up to 41% at times) to the southeast Atlantic during MIS3 (Fig. 3 *D* and *E*).

^{232}Th concentrations are on average 17 ppm for our Antarctic endmember, which is much higher than the global average of 11 ppm and nearly twofold higher than the 9 ppm found in Patagonia (36, 37). Elevated Antarctic Th concentrations may be a reason for the higher Th fluxes measured at our core site during MIS3 (Fig. 4*A*). Assuming ^{232}Th of 17 ppm (37) for the Antarctic endmember, we estimate Antarctica contributed an average of 0.10 g cm^{-2} ka^{-1} of lithogenic fraction during MIS3 (Fig. 3*F*). Lithogenic flux-by-source estimates from Antarctica at each "camel hump" peak at ~52 and ~42 ka with 0.17 and 0.23 g cm^{-2} ka^{-1}, respectively (Fig. 3*F*).

There are several additional lines of evidence that strongly indicate IRD is responsible for the MIS3 camel humps in TN057-6. In both the North (62) and South Atlantic (63), higher grain sizes have been used to identify IRD fractions. Recent analyses of ODP 1090 revealed that the mean grain size and the percentage of grains between 10 and 63 μm increased during MIS3, meaning grains larger than 10 μm were responsible for the increase in mean grain size, which varied synchronously with the higher lithogenic flux (Fig. 4 *A*, *C*, and *D*) (38). Moreover, n-alkane fluxes, a proxy representative of continental inputs derived from the leaf wax of terrestrial vegetation, were lower during MIS3 compared to MIS4 and 2, therefore while lithogenic fluxes were highest during MIS3, the n-alkane data indicate a decrease in the contribution of aeolian and fluvial material during MIS3 (*SI Appendix*, Fig. S5) (20). While there are only three MIS3 n-alkane data points, if they are representative, they indicate that fluxes of n-alkane decreased approximately threefold to fourfold from MIS4 to MIS3. In contrast to MIS3, both n-alkane and lithogenic fluxes are high during MIS2 and MIS4 glacial maxima. Together, these data suggest a source input type with larger particle diameters, like IRD, that did not originate from vegetated terrigenous area is responsible for material deposited to the southeast Atlantic during the MIS3 lithogenic flux maxima.

Evidence of a nonaeolian source during MIS3 is supported by a comparison of lithogenic fluxes across other core sites in the South Atlantic. During MIS3, fluxes at PS2498-1 on the Mid-Atlantic Ridge are essentially the same magnitude as fluxes measured at TN057-6 (*SI Appendix*, Fig. S6) (16). If the source was Patagonian dust, then the Mid-Atlantic Ridge site would have had higher fluxes because it is closer to Patagonia. This is evident during glacial periods when fluxes are higher on the Mid-Atlantic Ridge than in the southeast Atlantic. Therefore, similar lithogenic flux magnitudes at both Atlantic sites suggest that Patagonian dust is the source during MIS2 and 4 but not during MIS3. Antarctic IRD is a plausible source because Antarctic icebergs may pass over the Mid-Atlantic Ridge en route to the southeast Atlantic, meaning IRD could contribute to lithogenic fluxes at both sites.

By comparing lithogenic fluxes between the Atlantic and Pacific sectors of the Southern Ocean, we further rule out variability in South American dust supply as a source during MIS3. Lithogenic fluxes during glacial periods in both the Pacific and Atlantic sectors increase synchronously (2). During MIS3, however, fluxes measured at core sites in the Pacific do not mirror Atlantic patterns. More specifically, while Atlantic fluxes during MIS3 are greater than during glacial periods, Pacific fluxes during MIS3 do not outpace those during glacials (2) (Fig. 4*E*). This indicates that the source responsible for

the MIS3 camel humps only impacted the Atlantic, and not the Pacific. This line of evidence further excludes SSA dust.

In addition, IRD has been shown to be present during MIS3 in sediment records at three sites (TN057-21, TN057-10, and TN057-13) in the Atlantic sector of the Southern Ocean (Fig. 1) (61). Increases in IRD, determined by mineralogical and grain size analysis at these sites, are synchronous with increases in our lithogenic flux record during MIS3 (61), further indicating that IRD contributes to our core site. Antarctic IRD has also been shown to be a source of sediment to the Scotia Sea during the last glacial termination, MIS3 (28, 64), and potentially during other warm glacial periods (65). Recent model trajectory analysis also supports the long-range transit of icebergs from Antarctica to as far north as 42°S, the same latitude as TN057-6, during the preindustrial period (7), thus it can be expected that IRD reached this site during MIS3.

The composition of our Antarctic endmember is defined from bedrock samples surrounding the Ross Sea Ice Shelf (37), which is in the Pacific sector of the Southern Ocean and an unlikely source for TN057-6 IRD. A more likely source location for TN057-6 is the ice flowing into the southern Weddell Sea, based on our following reasoning. While modern remote sensing shows that icebergs from the Ross Sea can reach the South Atlantic, far more originate from the Weddell Sea (66), which is in the Atlantic sector and closer to the southeast Atlantic. In order for the ice draining into the Weddell Sea to be the source of IRD, the Weddell Sea IRD would need to have similar isotopic compositions to the Ross Sea bedrock samples. We can expect similarities in the Sr-Nd-Pb systematics between the two sites because the crustal ages and compositions of the bedrock are continuous, and both are the termini for ice draining from East (Transantarctic Mountains) and West Antarctica (67). Unfortunately, there are few published analyses of bedrock samples or subglacial sediments on the southern side of the Weddell Sea for comparison, or appropriate Weddell Sea core samples. Indeed, an Sr isotope ratio from one sample (68) and Nd isotopes from two samples (68, 69) from the southern Weddell Sea show similar values to those found in the Ross Sea Ice Shelf. Our geochemical results are in line with inferences from Starr et al. (7), who concluded, using indirect mineralogical evidence, that IRD in the South Atlantic near southern Africa originated from the southern Weddell Sea.

We can rule out contributions from Patagonian IRD to the southeast Atlantic during MIS3 due to the major isotopic differences between the Patagonian endmember and our MIS3 samples (Fig. 2), but SSA IRD may be important in the Scotia Sea during glacial periods (70). Other Antarctic source areas, such as the Amundsen Sea and other locations in East and West Antarctica (65), do not have overlapping isotopic compositions with the TN057-6 MIS3 samples. Additionally, mineralogical provenance analysis from PS97085-3 in the Drake Passage shows no influence of Antarctic IRD during MIS3 (71). These observations, in combination with the lack of an IRD signal in the Pacific (43) (Fig. 4*E*), indicate the source of IRD to the southeast Atlantic originated downstream of the Drake Passage. This leaves either the Antarctic Peninsula or the Weddell Sea as potential source locations. There are many samples with published isotope data from the Antarctic Peninsula, but the overwhelming majority of isotopic data show high ε_{Nd} and low $^{87}Sr/^{86}Sr$ ratios compared to our MIS3 samples (72), leaving the Weddell Sea geochemically and geographically as the most likely source.

Mechanism for Suborbital Fluctuations in IRD Transport to the Southeastern Atlantic during MIS3. We have shown multiproxy evidence supporting our hypothesis that Antarctic IRD from the Weddell Sea episodically supplied material to the southeast Atlantic during MIS3. These results raise additional questions. What triggered IRD transport to the southeast Atlantic and what does it say about Antarctic ice sheet dynamics and SH climate during MIS3? And did these events have impacts on biogeochemical cycles?

We hypothesize the impetus for suborbital increases in IRD from Antarctica to the southeast Atlantic was SH climate shifts. Specifically, we link our results to abrupt millennial-scale warmings, Antarctic Isotope Maximum (AIM) events, that document increased SH temperatures which would have initiated ice sheet instability and iceberg discharge into the Weddell Sea. The vertical shading in Fig. 5 highlights the timing of the three major AIM events (14, 12, 8) associated with the "camel hump" interval. Each AIM event lasted for ~2.5 ky (41) and was characterized by an increase in Antarctic temperature as well as in sea surface temperatures (SSTs), with a median increase of 0.7 °C across the Southern Ocean and a median increase of 2 °C at TN057-6 (73). Ice sheet margins feeding into the Weddell Sea likely responded to changes in Antarctic temperatures and SSTs, allowing for melting and increased iceberg discharge.

Increased SH temperatures during the AIM events had a number of effects on ocean and climate conditions, some of which are reflected in our isotopic data as well as by other proxies. Following the AIM events, there was an increase in the lithogenic flux (Fig. 5*A*), grain size (Fig. 5*B*), and the contribution of material from Antarctica (Fig. 5*C*). These results suggest that marginal ice sheet instability likely led to increased iceberg discharge and related increases in IRD from Antarctica delivered to the South Atlantic. There appears to be a 1 to 4 ky lag between maximum Antarctic temperatures and the peak lithogenic fluxes measured at TN057-6 (Fig. 5 *A* and *H*). At face value and recognizing that there may be chronological offsets between the ice core and TN057-6, this lag time seems to reflect a plausible response time of the ice margin to the initial warming. Our hypothesis, highlighting the role of millennial-scale AIM events and their impacts on the high latitude southern cryosphere, explains both the unexpected pattern and magnitude of lithogenic fluxes to the South Atlantic Ocean observed during MIS3.

Interestingly, there is not a corresponding increase in lithogenic flux after AIM8, which may be due to the SH mid-latitudes reaching persistent, near-peak glacial conditions between 40 and 30 ka. In both Patagonia and New Zealand, glaciers expanded to full glacial maximum limits before ~40 ka, and repeatedly before 30 ka, consistent with marine proxy records from the Southern Ocean (74–76). Thus, the near peak glacial conditions in the SH after AIM8 may have prevented further ice sheet instability in Antarctica, resulting in less IRD reaching the southeast Atlantic. This is in line with decreasing mean grain sizes after ~38 ka (Figs. 4 *C* and *D* and 5*B*), suggesting that large grain sizes, such as those associated with IRD, did not reach our core site.

Our hypothesis might imply similar instances of IRD intrusion during the last termination. Indeed, thermal forcings in the SH have also been invoked to cause increased IRD in the Scotia Sea after the LGM (6, 77, 78). We do not, however, observe such a signal at TN057-6 during the last glacial termination. Our isotopic results combined with the grain size data indicate that these IRD intrusions did not reach the southeast Atlantic, suggesting that our core site was not sensitive to Antarctic ice sheet instability during the last deglaciation or that there were different underlying modes of instability between MIS3 and the last deglaciation.

We suggest that the intermediate temperature conditions during parts of MIS3 compared to other intervals (e.g., MIS2 and MIS4), particularly before 40 ka, allowed for millennial-scale Antarctic climate warmings to impact the Antarctic ice sheets margins.

During these times, conditions during MIS3 were warm enough for Antarctica to "feel" warm AIM events and to provide the impetus for ice sheet discharge, but cool enough in the Southern Ocean to allow for the transport of icebergs to distal sites such as TN057-6.

Impacts of IRD on Biogeochemical Cycles during MIS3. We compare our results to previously published records of nutrient utilization and export production from ODP 1090 (18) and the new, highly resolved CO_2 record from the WAIS Divide (39) to evaluate the potential impact of IRD on productivity, Fe supply, and atmospheric CO_2. Following each AIM event, lithogenic fluxes and Antarctic IRD contributions were synchronous with increases in soluble Fe (Fig. 5 *A*–*D*). We hypothesize that Antarctic IRD was a source of this additional Fe, which could have aided in relieving Fe limitation in the subantarctic Southern Ocean. Following each AIM event, increases in the IRD-derived lithogenic fluxes and soluble Fe were also in phase with $\delta^{15}N$ values, a proxy of nutrient utilization, and alkenone fluxes, a paleoproductivity indicator. In fact, alkenone fluxes reached up to 800 ng cm^{-2} ka^{-1} after AIM14, which is higher than fluxes measured during MIS4 or MIS2. IRD is a particularly efficient source of soluble (bioavailable) Fe as ice sheets expose new mechanically weathered primary silicates with Fe(2+) (33, 79). It therefore seems plausible that the delivery of IRD-associated Fe fertilized the subantarctic South Atlantic during these post-AIM periods, as illustrated by concurrent maxima in nutrient utilization (Fig. 5*E*) and alkenone fluxes (Fig. 5*F*).

While previous studies have suggested that aeolian dust drove these millennial-scale MIS3 CO_2 variations (18), our isotopic results point to IRD as an additional source (Fig. 5*G*). It is important to note, however, that high alkenone fluxes could also be explained by climate-related changes in ocean stratification leading to low oxygen conditions (80), which would have increased during non-AIM intervals, trapping CO_2 in the deep sea and lowering deep water oxygen concentrations (81). Yet these physical changes in ocean dynamics might have occurred concurrently with productivity changes from Fe supplied by IRD (35).

Conclusions

Our record documents that dynamic changes in atmospheric and cryospheric SH climate occurred over the past 150 ka. Patagonian dust alone contributed up to 59% of the <5 μm fraction of the lithogenic material to the subantarctic Southern Ocean during glacial periods MIS2, 4, and 6 (and up to 68% during the LGM), while lithogenic material originating from southeastern Africa increased in relative importance as a source during interglacials MIS1, and 5. Samples from MIS3 show a unique Sr-Nd-Pb isotopic signature that is best explained by contributions of Antarctic IRD likely from the Weddell Sea. We linked intrusions of this IRD to millennial-scale warm events in the SH that we suggest caused marginal ice sheet instability and iceberg transport to TN057-6. The IRD contributed up to 41% of the total lithogenic flux at times of greatest IRD contribution during MIS3. In addition, we conclude that periods of high IRD were synchronous with high biologic nutrient utilization and high primary production that were likely promoted by high soluble Fe fluxes associated with the IRD that could have played a role in decreased atmospheric CO_2. Overall, our work highlights the interconnectedness of multiple Earth Systems in the SH over the past 150 ka.

Methods and Materials

We processed Sr, Nd, and Pb isotope ratios of the <5 μm fraction of 57 samples from sediment core TN057-6 (42°54′S, 8°54′E, 3,751 m), located in the southeast Atlantic subantarctic zone (Fig. 1). TN057-6 was chosen because it has a robust age model (15, 16), it is located downwind of SSA dust sources (17), and the site is on the Agulhas Ridge, above the deep Cape Basin abyssal plain, and thus is not impacted by horizontal abyssal flow of sediment by bottom currents. Additionally, its parallel core ODP Site 1090 also has a robust age model and many complementary paleoproxies are published, including ^{230}Th-normalized dust flux reconstructions and grain size analyses (18, 38). Our sampling of TN057-6 covers a time period between 146 and 8 ka BP with a time resolution that varied but averaged ~3 ky with higher-resolution sampling (~1 ky) during MIS3. In addition, we present data on Holocene and LGM samples from four cores off the coast of southeastern Africa beneath the Agulhas Current (RC11-86, RC17-69, VM14-77, and VM19-214). These data are in line with Sr and Nd isotope ratios from Franzese et al. (12).

To constrain the Sr, Nd, and Pb isotopic compositions of the Patagonian endmember, we present new data on 62 samples collected between 46°S and 54°S in SSA (*SI Appendix*, Fig. S1). Glacial and nonglacial samples were collected below the surface or soil horizon from moraines, outwash plains, glaciolacustrine sections, and other geomorphic settings. Most samples represent sediments deposited during and since MIS2; in addition, some samples are between the LGM and ~1 Ma (*SI Appendix*, Fig. S7). More information can be found in *SI Appendix* and Datasets S1 and S2.

Sampling Processing. For marine sediment core samples, the continental lithogenic fraction was separated from bulk sediment following published procedures at Lamont-Doherty Earth Observatory (LDEO) (11). Briefly, the <5 μm fraction was obtained through gravitational settling. Only the <5 μm fraction was used in analyses, taking into account that small particles predominate in wind-blown dust, and that Sr ratios tend to be higher in the small particle size fraction of PSA samples because clays and micas often have high Rb/Sr ratios. Additionally, using the <5 μm fraction allows easy comparison with previous provenance studies that use the <5 μm fraction (e.g., refs. 12, 23, 42, 47, and 48). Samples were processed using a sequential leaching method to remove organics, carbonates, and ferromanganese (oxy-)hydroxides (82). The PSA samples from SSA were processed in the same manner as the sediment core samples and only the <5 μm fraction was used, except in instances with no or fewer than 2 samples from subareas within the Northern SSA PSA (see *SI Appendix* for more details). In fact, a plot of the Nd-Sr isotope ratios of the new PSA samples clearly indicates that the <5 μm samples have higher Sr isotope ratios than the coarser <63 μm samples, while Nd isotopes show no bias (*SI Appendix*, Fig. S8). These samples were subsequently digested using concentrated Optima grade HF-HNO_3 with $HClO_4$ as needed to remove organic material and Sr, Nd, and Pb were separated, all following standard procedures at LDEO (11). Prior to separation, an aliquot of each SSA sample was obtained for elemental concentration.

Sr-Nd-Pb Isotopic Analysis. Sr, Nd, and Pb isotope ratios were measured on a ThermoScientific Neptune Plus MC-ICP-MS at LDEO using static multicollection. $^{87}Sr/^{86}Sr$ and $^{143}Nd/^{144}Nd$ isotope ratios were corrected for instrumental mass fractionation using the exponential mass fractionation law, assuming $^{86}Sr/^{88}Sr = 0.1194$ and $^{146}Nd/^{144}Nd = 0.7219$. Pb samples were spiked with thallium (Tl) to achieve a Pb/Tl ratio of ~5.4. Tl isotopes were used to correct for mass fractionation using the exponential fractionation law and assuming $^{203}Tl/^{205}Tl = 0.41844$ (83). All the sample analyses were bracketed by measurements of the following reference materials and the data are corrected using the following values: NIST SRM 987 ($^{87}Sr/^{86}Sr = 0.710240$) and JNdi [$^{143}Nd/^{144}Nd = 0.512115$ (84)], SRM NBS 981 [16.9405, 15.4963, and 36.7219 for $^{206}Pb/^{204}Pb$, $^{207}Pb/^{204}Pb$, and $^{208}Pb/^{204}Pb$, respectively (85)]. Reported analytical errors in the data tables represent the propagated 2 SE internal analytical measurement uncertainties and the external uncertainty based on the variability of the bracketing standards, corrected for instrumental drift, during each run session, and is calculated as square root [(internal error)^2+(external error)^2]. USGS rock standard BCR-2 was also digested in the same manner as the core samples and analyzed as an independent measure of sample reproducibility. Measured BCR-2 values for Nd and Pb isotopes were $^{143}Nd/^{144}Nd = 0.512631 \pm 10$, n = 10, 6 run sessions; $^{206}Pb/^{204}Pb = 18.7555 \pm 190$, n = 10, $^{207}Pb/^{204}Pb = 15.6198 \pm 152$, n = 11, $^{208}Pb/^{204}Pb = 38.7146 \pm 650$, n = 10, 8 run sessions. These uncertainties are the 2σ variability of the BCR-2 results after filtering 2σ outliers, and shown in terms of the last digits of the listed isotope ratio values. For Sr isotopes, the results are

$^{87}Sr/^{86}Sr = 0.705013 \pm 24$, n = 9 for the samples measured over 6 of the 7 run sessions. These Sr and Nd isotope results are within 2σ of published values (86). Sr isotopes on 2 BCR-2 samples measured during a 7th run session showed an average value 0.704906, outside of the 2σ range of the other 6 run sessions. The TN057-6 samples measured during that session are marked in Dataset S1. While the BCR-2 results for that session may indicate a bias in the Sr isotope ratios for those samples, it is negligible compared to the large Sr isotope variability of the samples. Moreover, taking into account that the Pb in the BCR-2 rock standard has been shown to be inhomogeneously contaminated, and no steps were taken to leach out the contaminant, the Pb isotope ratios are within published results (86). Nd isotope data are reported here in units of ($\varepsilon_{Nd}(0)$= ([$^{143}Nd/^{144}Nd_{(measured)}/^{143}Nd/^{144}Nd_{(CHUR)}$]−1]∗$10^4$), the deviation in parts per 10,000 from the CHUR value ("chondritic uniform reservoir," an estimate of the average $^{143}Nd/^{144}Nd$ of the solar system). Here, we use 0.512638 (87) in order to be consistent with decades of past data, rather than the updated value of 0.512630 (88). We note that the difference is small, only 0.16 ε_{Nd} units, and both values are within analytical error. Sr, Nd, and Pb concentrations in Patagonian samples were measured on a VG PQ ExCell quadrupole ICP-MS following standard procedure at LDEO (11). Additional details can be found in *SI Appendix*.

Isotopic Mixture Modeling. The isotopic mixing model MixSIAR was employed to quantify the relative contribution of each source area to a sample and takes into account isotopic variability of each endmember (89). MixSIAR has previously been used to quantify source contribution in modern-day dust (49) and paleoprovenance (44) studies. The model solves a mass balance equation for a three-isotope system. The uncertainty of the model output is derived from the isotopic variability of each endmember included as a source in the model (*SI Appendix*, Table S1), with individual source contributions typically <±0.5% (47). Due to the nonlinear mixing relationships between Sr-Nd-Pb isotopic systems, elemental concentrations were also incorporated (*SI Appendix*, Table S2).

Three parallel chains of Markov Chain Monte Carlo simulation outputs were run on "normal" mode in MixSIAR, discarding the first 50,000 iterations and retaining the final 100,000. Convergence was achieved when the Gelman–Rubin diagnostic was between 1.0 and 1.05 and the Geweke diagnostic was equal to 0 for the three parallel chains. Samples that did not reach convergence on the "normal" mode and were run on the "long" mode, discarding 200,000 iterations and retaining the final 300,000. The posterior distributions of these runs were then combined across the three chains for 3,000 total values.

Data, Materials, and Software Availability. Dataset S1 contains the Sr, Nd, and Pb isotope compositions of sediments collected from TN057-6 and the new data from the four cores near southeastern Africa under the Agulhas Current. Dataset S2 contains 62 Patagonian samples newly presented in this work. Datasets S1 and S2 are archived in the EarthChem Library at: https://doi.org/10.60520/IEDA/113252 (90) and https://doi.org/10.60520/IEDA/113253 (91), respectively. The R package MixSIAR, v3.1 used in this work was run in RStudio, v.4.3.2. The code used in this work can be found in Barkley et al. (49) and in the University of Miami Data Repository: https://doi.org/10.17604/qqq0-p310 (92). All study data are included in the article and/or supporting information.

ACKNOWLEDGMENTS. A.E.B. acknowledges support from a Lamont Postdoctoral Fellowship. G.W. and J.L.M. thank the Vetlesen Foundation for their support. C.R. acknowledges a Swiss NSF Postdoctoral Fellowship. C.R. and M.R.K. thank the LDEO Climate Center and NASA-GISS for funding support. B.G.K. acknowledges the NSF Postdoctoral Fellowship (OPP 1204050). R.F.A. acknowledges NSF support, primarily by OCE 0823507. S.L.G. acknowledges the Storke Endowment of the Department of Earth and Environmental Sciences, Columbia University. We thank Dr. Shannon Doherty for her helpful insights and contributions regarding the mixing model. The views expressed in this work are those of the authors and do not necessarily represent the views or policies of the United States Environmental Protection Agency.

Author affiliations: [a]Division of Geochemistry, Lamont-Doherty Earth Observatory of Columbia University, Palisades, NY 10964; [b]Department of Earth and Environmental Sciences, Columbia University, New York, NY 10027; [c]Department of Geology, Colby College, Waterville, ME 04901; [d]Centro de Investigaciones en Ciencias de la Tierra, Ciudad Universitaria, Córdoba X5016CGA, Argentina; [e]Nanjing Institute of Geology and Palaeontology and Center for Excellence in Life and Paleoenvironment, Chinese Academy of Sciences, Nanjing 210008, China; [f]Marine Isotope Geochemistry, Institute for Chemistry and Biology of the Marine Environment, Carl von Ossietzky Universität Oldenburg, Oldenburg 26129, Germany; and [g]Department of Geography and Environmental Sciences, Northumbria University, Newcastle-upon-Tyne NE1 8ST, United Kingdom

Author contributions: G.W., C.R., M.R.K., and S.L.G. designed research; C.R., B.G.K., F.C., Y.C., and L.B. performed research; A.E.B. contributed new reagents/analytic tools; A.E.B., G.W., C.R., M.R.K., J.L.M., R.F.A., J.L., and S.L.G. analyzed data; and A.E.B., G.W., M.R.K., J.L.M., R.F.A., and S.L.G. wrote the paper.

The authors declare no competing interest.

This article is a PNAS Direct Submission.

1. G. Winckler, R. F. Anderson, M. Q. Fleisher, D. McGee, N. M. Mahowald, Covariant glacial-interglacial dust fluxes. *Science* **320**, 93–96 (2008).
2. F. Lamy *et al.*, Increased dust deposition in the Pacific Southern Ocean during glacial periods. *Science* **343**, 403–407 (2014).
3. F. Lambert, M. Bigler, J. P. Steffensen, M. Hutterli, H. Fischer, Centennial mineral dust variability in high-resolution ice core data from Dome C, Antarctica. *Clim. Past* **8**, 609–623 (2012).
4. J. H. Martin, Glacial-interglacial CO2 change: The iron hypothesis. *Paleoceanography* **5**, 1–13 (1990).
5. I. Tegen, R. Miller, A general circulation model study on the interannual variability of soil dust aerosol. *J. Geophys. Res.* **103**, 25975–25995 (1998).
6. M. E. Weber *et al.*, Millennial-scale variability in Antarctic ice-sheet discharge during the last deglaciation. *Nature* **510**, 134–138 (2014).
7. A. Starr *et al.*, Antarctic icebergs reorganize ocean circulation during Pleistocene glacials. *Nature* **589**, 236–241 (2021).
8. B. Delmonte *et al.*, Comparing the Epica and Vostok dust records during the last 220,000 years: Stratigraphical correlation and provenance in glacial periods. *Earth Sci. Rev.* **66**, 63–87 (2004).
9. S. R. Hemming, Heinrich events: Massive late Pleistocene detritus layers of the North Atlantic and their global climate imprint. *Rev. Geophys.* **42**, RG1005 (2004).
10. A. M. Franzese, S. R. Hemming, S. L. Goldstein, Use of strontium isotopes in detrital sediments to constrain the glacial position of the Agulhas retroflection. *Paleoceanography* **24**, 1–12 (2009).
11. B. G. Koffman *et al.*, Abrupt changes in atmospheric circulation during the Medieval Climate Anomaly and Little Ice Age recorded by Sr-Nd isotopes in the Siple Dome Ice Core, Antarctica. *Paleoceanogr. Paleoclimatol.* **38**, e2022PA004543 (2023).
12. A. M. Franzese, S. R. Hemming, S. L. Goldstein, R. F. Anderson, Reduced Agulhas Leakage during the Last Glacial Maximum inferred from an integrated provenance and flux study. *Earth Planet. Sci. Lett.* **250**, 72–88 (2006).
13. T. L. Noble *et al.*, Greater supply of Patagonian-sourced detritus and transport by the ACC to the Atlantic sector of the Southern Ocean during the last glacial period. *Earth Planet. Sci. Lett.* **317–318**, 374–385 (2012).
14. F. Beny *et al.*, Radiogenic isotopic and clay mineralogical signatures of terrigenous particles as water-mass tracers: New insights into South Atlantic deep circulation during the last termination. *Quat. Sci. Rev.* **228**, 106089 (2020).
15. D. A. Hodell, C. D. Charles, F. J. Sierro, Late Pleistocene evolution of the ocean's carbonate system. *Earth Planet. Sci. Lett.* **192**, 109–124 (2001).
16. R. F. Anderson *et al.*, Biological response to millennial variability of dust and nutrient supply in the Subantarctic South Atlantic Ocean. *Philos. Trans. R. Soc. A Math. Phys. Eng. Sci.* **372**, 20130054 (2014).
17. S. Albani, N. M. Mahowald, B. Delmonte, V. Maggi, G. Winckler, Comparing modeled and observed changes in mineral dust transport and deposition to Antarctica between the Last Glacial Maximum and current climates. *Clim. Dyn.* **38**, 1731–1755 (2012).
18. A. Martínez-García *et al.*, Iron fertilization of the Subantarctic Ocean during the Last Ice Age. *Science* **343**, 1347–1350 (2014).
19. A. Martínez-García *et al.*, Links between iron supply, marine productivity, sea surface temperature, and CO2 over the last 1.1 Ma. *Paleoceanography* **24**, 1–14 (2009).
20. A. Martínez-García *et al.*, Southern Ocean dust-climate coupling over the past four million years. *Nature* **476**, 312–315 (2011).
21. I. Basile *et al.*, Patagonian origin of glacial dust deposited in East Antarctica (Vostok and Dome C) during glacial stages 2, 4 and 6. *Earth Planet. Sci. Lett.* **146**, 573–589 (1997).
22. F. E. Grousset *et al.*, Antarctic (Dome C) ice-core dust at 18 k.y. B.P.: Isotopic constraints on origins. *Earth Planet. Sci. Lett.* **111**, 175–182 (1992).
23. B. Delmonte *et al.*, Geographic provenance of aeolian dust in East Antarctica during Pleistocene glaciations: Preliminary results from Talos Dome and comparison with East Antarctic and new Andean ice core data. *Quat. Sci. Rev.* **29**, 256–264 (2010).
24. J. M. Prospero, J. E. Bullard, R. Hodgkins, High-latitude dust over the North Atlantic: Inputs from Icelandic proglacial dust storms. *Science* **335**, 1078–1082 (2012).
25. D. E. Sugden, R. D. McCulloch, A. J. M. Bory, A. S. Hein, Influence of Patagonian glaciers on Antarctic dust deposition during the last glacial period. *Nat. Geosci.* **2**, 281–285 (2009).
26. K. E. Kohfeld *et al.*, Southern Hemisphere westerly wind changes during the Last Glacial Maximum: Paleo-data synthesis. *Quat. Sci. Rev.* **68**, 76–95 (2013).
27. B. R. Markle, E. J. Steig, G. H. Roe, G. Winckler, J. R. McConnell, Concomitant variability in high-latitude aerosols, water isotopes and the hydrologic cycle. *Nat. Geosci.* **11**, 853–859 (2018).
28. B. Diekmann, G. Kuhn, Provenance and dispersal of glacial-marine surface sediments in the Weddell Sea and adjoining areas, Antarctica: Ice-rafting versus current transport. *Mar. Geol.* **158**, 209–231 (1999).
29. J. Weis *et al.*, One-third of Southern Ocean productivity is supported by dust deposition. *Nature* **629**, 603–608 (2024).
30. A. W. Schroth, J. Crusius, E. R. Sholkovitz, B. C. Bostick, Iron solubility driven by speciation in dust sources to the ocean. *Nat. Geosci.* **2**, 337–340 (2009).
31. B. G. Koffman *et al.*, Glacial dust surpasses both volcanic ash and desert dust in its iron fertilization potential. *Global Biogeochem. Cycles* **35**, e2020GB006821 (2021).

32. E. M. Shoenfelt, G. Winckler, F. Lamy, R. F. Anderson, B. C. Bostick, Highly bioavailable dust-borne iron delivered to the Southern Ocean during glacial periods. *Proc. Natl. Acad. Sci. U.S.A.* **115**, 11180–11185 (2018).
33. J. R. Hawkings *et al.*, Biolabile ferrous iron bearing nanoparticles in glacial sediments. *Earth Planet. Sci. Lett.* **493**, 92–101 (2018).
34. R. Raiswell *et al.*, Potentially bioavailable iron delivery by iceberg-hosted sediments and atmospheric dust to the polar oceans. *Biogeosciences* **13**, 3887–3900 (2016).
35. J. Gottschalk *et al.*, Biological and physical controls in the Southern Ocean on past millennial-scale atmospheric CO2 changes. *Nat. Commun.* **7**, 11539 (2016).
36. D. McGee *et al.*, Tracking eolian dust with helium and thorium: Impacts of grain size and provenance. *Geochim. Cosmochim. Acta* **175**, 47–67 (2016).
37. G. L. Farmer, K. Licht, R. J. Swope, J. T. Andrews, Isotopic constraints on the provenance of fine-grained sediment in LGM tills from the Ross Embayment, Antarctica. *Earth Planet. Sci. Lett.* **249**, 90–107 (2006).
38. M. van der Does *et al.*, Opposite dust grain-size patterns in the Pacific and Atlantic sectors of the Southern Ocean during the last 260,000 years. *Quat. Sci. Rev.* **263**, 106978 (2021).
39. T. Bauska, S. Marcott, E. Brook, Abrupt changes in the global carbon cycle during the last glacial period. *Nat. Geosci.* **14**, 91–96 (2021).
40. F. Parrenin *et al.*, Synchronous change of atmospheric CO2 and Antarctic temperature during the last deglacial warming. *Science* **339**, 1060–1063 (2013).
41. J. B. Pedro *et al.*, Beyond the bipolar seesaw: Toward a process understanding of interhemispheric coupling. *Quat. Sci. Rev.* **192**, 27–46 (2018).
42. D. M. Gaiero, Dust provenance in Antarctic ice during glacial periods: From where in southern South America? *Geophys. Res. Lett.* **34**, 1–6 (2007).
43. T. Struve *et al.*, A circumpolar dust conveyor in the glacial Southern Ocean. *Nat. Commun.* **11**, 5655 (2020).
44. J. Longman, T. Struve, K. Pahnke, Spatial and temporal trends in mineral dust provenance in the South Pacific–Evidence from mixing models. *Paleoceanogr. Paleoclimatol.* **37**, e2021PA004 (2022).
45. S. Gili *et al.*, Provenance of dust to Antarctica: A lead isotopic perspective. *Geophys. Res. Lett.* **43**, 2291–2298 (2016).
46. S. Gili *et al.*, Glacial/interglacial changes of Southern Hemisphere wind circulation from the geochemistry of South American dust. *Earth Planet. Sci. Lett.* **469**, 98–109 (2017).
47. T. Struve *et al.*, Systematic changes in circumpolar dust transport to the Subantarctic Pacific Ocean over the last two glacial cycles. *Proc. Natl. Acad. Sci. U.S.A.* **119**, 1–10 (2022).
48. B. G. Koffman *et al.*, New Zealand as a source of mineral dust to the atmosphere and ocean. *Quat. Sci. Rev.* **251**, 106659 (2021).
49. A. E. Barkley *et al.*, Interannual variability in the source location of North African dust transported to the Amazon. *Geophys. Res. Lett.* **49**, e2021GL097344 (2022).
50. S. L. Goldstein, R. K. O'Nions, P. J. Hamilton, A Sm-Nd isotopic study of atmospheric dusts and particulates from major river systems. *Earth Planet. Sci. Lett.* **70**, 221–236 (1984).
51. R. L. Rutberg, S. L. Goldstein, S. R. Hemming, R. F. Anderson, Sr isotope evidence for sources of terrigenous sediment in the southeast Atlantic Ocean: Is there increased available Fe for enhanced glacial productivity? *Paleoceanography* **20**, 1–10 (2005).
52. F. J. C. Peeters *et al.*, Vigorous exchange between the Indian and Atlantic oceans at the end of the past five glacial periods. *Nature* **430**, 661–665 (2004).
53. B. M. Chase, M. E. Meadows, Late Quaternary dynamics of southern Africa's winter rainfall zone. *Earth Sci. Rev.* **84**, 103–138 (2007).
54. J.-B. W. Stuut, X. Crosta, K. van der Borg, R. R. Schneider, Relationship between Antarctic sea ice and southwest African climate during the late Quaternary. *Geology* **32**, 909–912 (2004).
55. J.-B. W. Stuut *et al.*, A 300-kyr record of aridity and wind strength in southwestern Africa: Inferences from grain-size distributions of sediments on Walvis Ridge, SE Atlantic. *Mar. Geol.* **180**, 221–233 (2002).
56. M. H. Simon *et al.*, Eastern South African hydroclimate over the past 270,000 years. *Sci. Rep.* **5**, 1–10 (2015).
57. S. Gili *et al.*, South African dust contribution to the high southern latitudes and East Antarctica during interglacial stages. *Commun. Earth Environ.* **3**, 1–12 (2022).
58. F. Li, P. Ginoux, V. Ramaswamy, Distribution, transport, and deposition of mineral dust in the Southern Ocean and Antarctica: Contribution of major sources. *J. Geophys. Res. Atmos.* **113**, 1–15 (2008).
59. C. Peltier *et al.*, The last two glacial cycles in central Patagonia: A precise record from the Ñirehuao glacier lobe. *Quat. Sci. Rev.* **304**, 107873 (2023).
60. F. E. Grousset, P. Rognon, G. Coudé-Gaussen, P. Pédemay, Origins of peri-Saharan dust deposits traced by their Nd and Sr isotopic composition. *Palaeogeogr. Palaeoclimatol. Palaeoecol.* **93**, 203–212 (1992).
61. S. L. Kanfoush *et al.*, Millennial-scale instability of the Antarctic Ice Sheet during the last glaciation. *Science* **288**, 1815–1818 (2000).
62. M. A. Prins *et al.*, Ocean circulation and iceberg discharge in the glacial North Atlantic: Inferences from unmixing of sediment size distributions. *Geology* **30**, 555–558 (2002).
63. M. van der Does *et al.*, Late Holocene dust deposition fluxes over the entire South Atlantic Ocean. *Geochem. Geophys. Geosyst.* **25**, e2023GC011105 (2024).
64. A. Hofmann, "Kurzfistige Klimaschwankungen im Scotiameer under Ergebnisse zur Kalbungsgeschichte der Antarktis während der letzten 200 000 Jahre," Bundesanstalt fuer Geowissenschaften und Rohstoffe, Hannover, Germany (1999).
65. I. Bailey *et al.*, Episodes of Early Pleistocene West Antarctic Ice Sheet retreat recorded by Iceberg Alley sediments. *Paleoceanogr. Paleoclimatol.* **37**, e2022PA004433 (2022).
66. T. Rackow *et al.*, A simulation of small to giant Antarctic iceberg: Differential impact on climatology estimates. *J. Geophys. Res. C Ocean.* **122**, 3170–3190 (2017).
67. J. B. Anderson, J. T. Andrews, Radiocarbon constraints on ice sheet advance and retreat in the Weddell Sea, Antarctica. *Geology* **27**, 179–182 (1999).
68. H. J. Walter, E. Hegner, B. Diekmann, G. Kuhn, M. M. Rutgers Van Der Loeff, Provenance and transport of terrigenous sediment in the South Atlantic Ocean and their relations to glacial and interglacial cycles: Nd and Sr isotopic evidence. *Geochim. Cosmochim. Acta* **64**, 3813–3827 (2000).
69. M. Roy, T. van de Flierdt, S. R. Hemming, S. L. Goldstein, 40Ar/39Ar ages of hornblende grains and bulk Sm/Nd isotopes of circum-Antarctic glacio-marine sediments: Implications for sediment provenance in the Southern Ocean. *Chem. Geol.* **244**, 507–519 (2007).
70. B. Diekmann *et al.*, "Terrigenous sediment supply in the polar to temperate South Atlantic: Land-ocean links of environmental changes during the Late Quaternary" in *The South Atlantic Late Quaternary: Reconstruction of Material Budgets and Current Systems*, G. Wefer, S. Mulitza, V. Ratmeyer, Eds. (Springer, 2010), pp. 375–399.
71. S. Wu *et al.*, Late Quaternary terrigenous sediment supply in the Drake Passage in response to Patagonian and Antarctic ice dynamics. *Global Planet. Change* **221**, 104024 (2023).
72. C. L. Blanchet, A database of marine and terrestrial radiogenic Nd and Sr isotopes for tracing earth-surface processes. *Earth Syst. Sci. Data* **11**, 741–759 (2019).
73. H. J. Anderson, J. B. Pedro, H. C. Bostock, Z. Chase, T. L. Noble, Compiled Southern Ocean sea surface temperatures correlate with Antarctic Isotope Maxima. *Quat. Sci. Rev.* **255**, 106821 (2021).
74. P. I. Moreno *et al.*, Radiocarbon chronology of the last glacial maximum and its termination in northwestern Patagonia. *Quat. Sci. Rev.* **122**, 233–249 (2015).
75. J. L. García *et al.*, The MIS 3 maximum of the Torres del Paine and Última Esperanza ice lobes in Patagonia and the pacing of southern mountain glaciation. *Quat. Sci. Rev.* **185**, 9–26 (2018).
76. A. M. Doughty *et al.*, Mismatch of glacial extent and summer insolation in Southern Hemisphere mid-latitudes. *Geology* **43**, 407–410 (2015).
77. A. Shemesh *et al.*, Sequence of events during the last deglaciation in Southern Ocean sediments and Antarctic ice cores. *Paleoceanography* **17**, 8-1–8-7 (2002).
78. B. Diekmann *et al.*, Terrigenous sediment supply in the Scotia Sea (Southern Ocean): Response to Late Quaternary ice dynamics in Patagonia and on the Antarctic Peninsula. *Palaeogeogr. Palaeoclimatol. Palaeoecol.* **162**, 357–387 (2000).
79. R. Raiswell, L. G. Benning, M. Tranter, S. Tulaczyk, Bioavailable iron in the Southern Ocean: The significance of the iceberg conveyor belt. *Geochem. Trans.* **9**, 1–9 (2008).
80. R. F. Anderson *et al.*, Deep-sea oxygen depletion and ocean carbon sequestration during the last ice age. *Global Biogeochem. Cycles* **33**, 301–317 (2019).
81. J. Gottschalk *et al.*, Southern Ocean link between changes in atmospheric CO2 levels and Northern-Hemisphere climate anomalies during the last two glacial periods. *Quat. Sci. Rev.* **230**, 106067 (2020).
82. R. A. Mortlock, P. N. Froelich, A simple method for the rapid determination of biogenic opal in pelagic marine sediments. *Deep Sea Res. Part A Oceanogr. Res. Pap.* **36**, 1415–1426 (1989).
83. M. Thirwall, Multicollector ICP-MS analysis of Pb isotopes using a 207Pb-204Pb double spike demonstrates up to a 400 ppm/amu systematic erros in Tl-normalization. *Chem. Geol.* **184**, 255–279 (2002).
84. T. Tanaka *et al.*, JNdi-1: A neodymium isotopic reference in consistency with La Jolla neodymium. *Chem. Geol.* **168**, 279–281 (2000).
85. S. J. G. Galer, W. Abouchami, Practical application of lead triple spiking for correction of instrumental mass discrimination. *Mineral. Mag.* **62A**, 491–492 (1998).
86. J. Jweda, L. Bolge, C. Class, S. L. Goldstein, High precision Sr-Nd-Hf-Pb isotopic compositions of USGS reference material BCR-2. *Geostand. Geoanalytical Res.* **40**, 101–115 (2016).
87. S. B. Jacobsen, G. J. Wasserburg, Sm-Nd isotopic evolution of chondrites. *Earth Planet. Sci. Lett.* **50**, 139–155 (1980).
88. A. Bouvier, J. D. Vervoort, P. Patchett, The Lu-Hf and Sm-Nd isotopic composition of CHUR: Constraints from unequilibrated chondrites and implications for the bulk composition of terrestrial planets. *Earth Planet. Sci. Lett.* **273**, 48–57 (2008).
89. B. C. Stock *et al.*, Analyzing mixing systems using a new generation of Bayesian tracer mixing models. *PeerJ* **2018**, 1–27 (2018).
90. A. E. Barkley *et al.*, Sr-Nd-Pb isotope ratios for marine sediment core TN057-6 in the southeast Atlantic Ocean and cores located under the Agulhas Current over the past 150,000 years, Version 1.0. Interdisciplinary Earth Data Alliance (IEDA). https://doi.org/10.60520/IEDA/113252. Accessed 17 May 2024.
91. A. E. Barkley *et al.*, Sr-Nd-Pb isotope ratios from potential aeolian dust sources in Patagonia, South America, Version 1.0. Interdisciplinary Earth Data Alliance (IEDA). https://doi.org/10.60520/IEDA/113253. Accessed 17 May 2024.
92. A. E. Barkley *et al.*, Data for Interannual variability in the source location of North African dust transported to the Amazon. University of Miami. https://doi.org/10.17604/QQQ0-P310. Accessed 17 May 2024.